

Generation of whistler waves by a rotating magnetic field source

A. V. Karavaev,^{1,a)} N. A. Gumerov,¹ K. Papadopoulos,¹ Xi Shao,¹ A. S. Sharma,¹ W. Gekelman,² A. Gigliotti,² P. Pribyl,² and S. Vincena²

¹*Department of Physics and Department of Astronomy, University of Maryland, College Park, Maryland 20742, USA*

²*Department of Physics and Astronomy, University of California, Los Angeles, California 90095, USA*

(Received 2 June 2009; accepted 24 November 2009; published online 6 January 2010)

The paper discusses the generation of polarized whistler waves radiated from a rotating magnetic field source created via a novel phased orthogonal two loop antenna. The results of linear three-dimensional electron magnetohydrodynamics simulations along with experiments on the generation whistler waves by the rotating magnetic field source performed in the large plasma device are presented. Comparison of the experimental results with the simulations and linear wave properties shows good agreement. The whistler wave dispersion relation with nonzero transverse wave number and the wave structure generated by the rotating magnetic field source are also discussed. The phase velocity of the whistler waves was found to be in good agreement with the theoretical dispersion relation. The exponential decay rate of the whistler wave propagating along the ambient magnetic field is determined by Coulomb collisions. In collisionless case the rotating magnetic field source was found to be a very efficient radiation source for transferring energy along the ambient magnetic field lines. © 2010 American Institute of Physics. [doi:10.1063/1.3274916]

I. INTRODUCTION

The interaction of rotating magnetic fields (RMFs) with plasmas is a fundamental plasma physics problem with implications to a wide range of areas, such as fusion related field-reversed configuration,^{1,2} space propulsion, precipitation of energetic particle population in Van Allen radiation belts,^{3,4} and near zone processes in pulsar magnetospheres. Earth itself is an example of a rotating magnetic dipole interacting with surrounding plasma. An important but not yet explored application of RMF is as efficient radiation source of magnetohydrodynamics (MHD) and whistler waves^{5,6} in space plasma. This application became more important after it was demonstrated that very low-frequency radio waves can precipitate Earth's inner radiation belt energetic electrons.^{7,8} The precipitation of electrons can happen through wave-particle resonant pitch angle scattering, when electrons satisfy the resonant condition,^{8,9}

$$\omega - k_{\parallel}v_{\parallel} = -\frac{n\Omega_{ce}}{\gamma}, \quad (1)$$

where ω is the wave frequency, k_{\parallel} is the wave number component along the magnetic field line, v_{\parallel} is the particle velocity component parallel to the magnetic field, Ω_{ce} is the electron cyclotron frequency, γ is the relativistic Lorentz factor, and n is an integer harmonic resonance number. On the other hand the electrons can be precipitated via a nonresonant scattering by creating nonlocal magnetic field gradient, which lead to breaking of the adiabatic invariant $\mu = v_{\perp}^2/B$, where v_{\perp} is the particle velocity component perpendicular to the magnetic field and B is the magnetic field value. The whistler and MHD waves created by the RMF source are candidates for creating such nonlocal magnetic field gradients.

Despite its importance, the basic plasma physics of the interaction of RMF with magnetoplasmas, the scaling laws that control it, and the range of potential applications to space plasma remain unexplored. To zeroth order, in a collisionless plasma a magnetic field rotating at a rate ω in a plasma drives a current due to the difference in mass of electrons and ions. Electrons quickly come to a corotational motion with RMF, generating a differential azimuthal current whose theoretical maximum, when all ions are stationary and all electrons are simultaneously involved in corotational motion, is given by $J_{\theta} = n\omega r$ (n is plasma density here).

The RMF can be generated either by a system of polyphase coils or by an actually rotating permanent or superconducting magnet (see Fig. 1). In Earth's magnetosphere, for example, in the equatorial region of $L=2$ the magnetic field is $\sim \mu T$, which yields a proton cyclotron frequency of tens of hertz. In laboratory plasmas confined by an ambient magnetic field the typical value is tens of gauss to several kilogauss, which corresponds to an ion cyclotron frequency Ω_{ci} in the range 10^4 – 10^6 Hz. In order to generate whistler waves, distinct from the MHD waves, we need to drive the RMF at a rate much faster than the ion cyclotron frequency. It is obvious that we can rotate a permanent magnet at a rate of tens or even hundreds of hertz, but it is impossible to do that at kilohertz or higher rates. In space experiments the first method is preferable since it does not need powerful energy supply in order to drive significant currents, while in the laboratory experiments we are forced to use the second one.¹⁰

Key questions about the interaction of the RMF with magnetized plasmas include the depth of penetration of the magnetic field into the plasma, the spatiotemporal structure of the induced waves as a function of the RMF and plasma parameters, and spatial decay rates of the perturbed magnetic field. In this paper we present a combination of analytic/

^{a)}Electronic mail: karavaev@umd.edu.

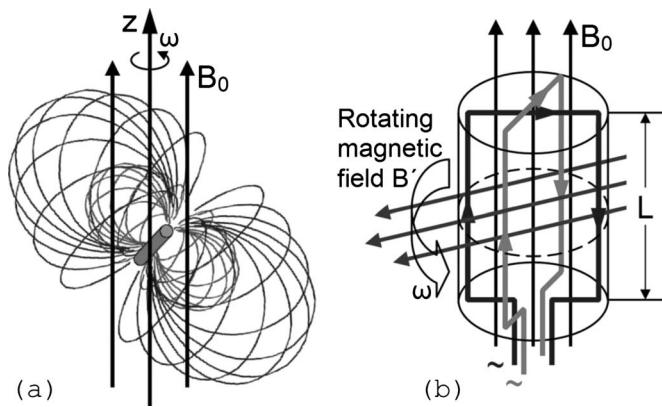


FIG. 1. Methods for creating a RMF in a magnetized plasma. The RMF can be generated either by (a) a rotating permanent magnet or (b) polyphase coils (superconducting or normal) with alternating phase shifted currents.

computational results along with experimental results from the large plasma device (LAPD) located at UCLA. These results highlight the generation of MHD (Ref. 10) and whistler waves in magnetized plasma by a RMF source.

II. EXPERIMENTS ON GENERATING WHISTLER WAVES BY THE RMF

The experiments on generating whistler waves in magnetized plasma by the RMF were performed in the upgraded large plasma device (LAPD-U) (Ref. 11) operated by the Basic Plasma Science Facility at the University of California, Los Angeles. The ambient magnetic field profile and the location of the probes and radiation source are shown in Fig. 2. The laboratory reference frame is oriented with the z -axis along the axis of the chamber and the y -axis pointing vertically upwards. Using a computer controlled data acquisition system in several cross sections of the machine (see Fig. 2), measurements of the three components of the perturbed magnetic field using three axis inductive loop magnetic pickup coil were performed on a square area with 25×25 points with 1 cm spacing. The probe features differentially wound loops that eliminate electrostatic pickup when used in conjunction with a differential amplifier. The loops are wound around a 1 mm cube with ten turns each. The cube is mounted within a glass tube and attached to a thin ceramic

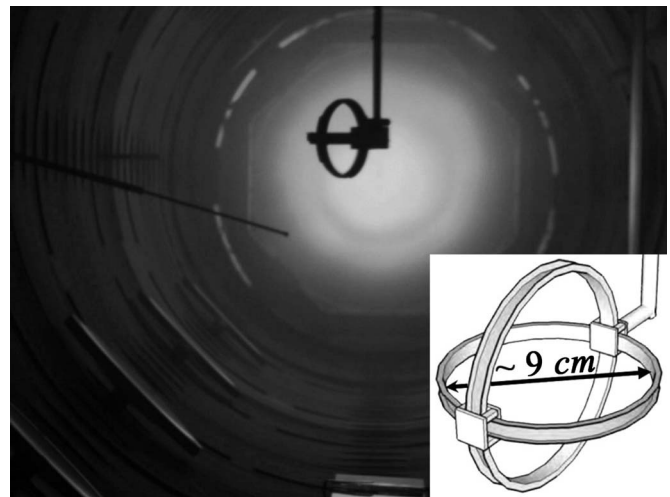


FIG. 3. The RMF antenna consisting of two independent coils approximately 9 cm in diameter with four turns each, shown inside the LAPD chamber. (The orientation of the antenna shown is not an actual orientation that was used in the experiments.) The three axis inductive magnetic pickup probe on the tip of the stainless steel shaft is also seen. Inset shows the design of the RMF antenna.

tube extending from the end of stainless steel probe shaft. The measurements were made in the 50 G region, which corresponds to cyclotron frequencies $\Omega_{ce} = 8.7 \times 10^8 \text{ s}^{-1}$ for electrons and $\Omega_{ci} = 1.21 \times 10^5 \text{ s}^{-1}$ for ions (used gas—He). The measurements closest to the radiation source were performed at distance $\sim 10 \text{ cm}$ (p35). The measurements farthest from the antenna were performed at distance $\sim 2.5 \text{ m}$ (p27). Average plasma density measured by a 56 GHz microwave interferometer was $n = 8.3 \times 10^{10} \text{ cm}^{-3}$. That corresponds to plasma frequency $\omega_{pe} = 1.62 \times 10^{10} \text{ s}^{-1}$ and electron skin-depth $d_e = c/\omega_{pe} = 1.85 \text{ cm}$.

A two-loop antenna (see Fig. 3) is placed inside the machine in such a way that the loops of the antenna are in the x - z and y - z planes, and centers of the loops were on the central axis of the chamber. The antenna consists of two independent coils $\sim 9 \text{ cm}$ in diameter ($\sim 5d_e$) and four turns each. Each coil has independent power supply (resonant adjustable LRC circuits) that can drive an alternating current with frequencies 50–500 kHz and current magnitude up to 500 A. The effect of mutual inductance between the coils is

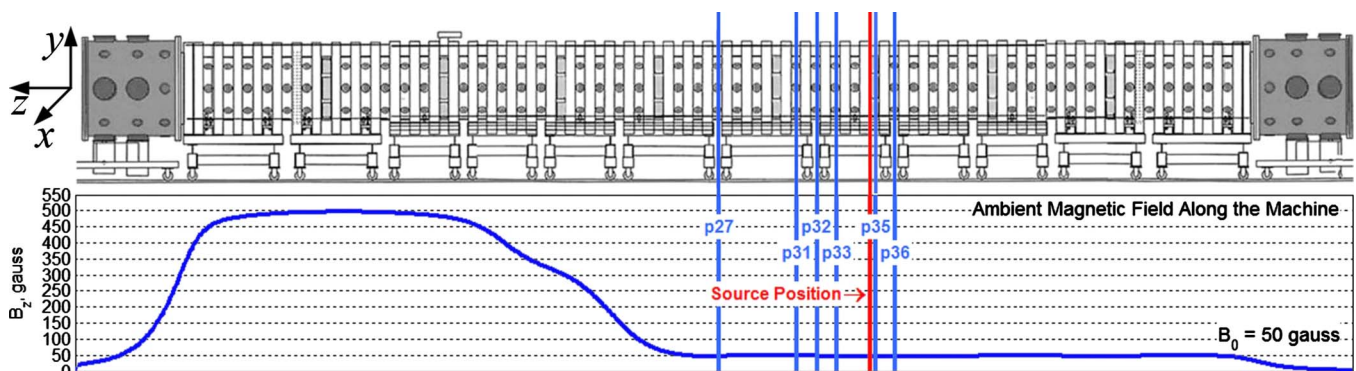


FIG. 2. (Color online) Ambient magnetic field profile along the chamber: p27, p31, p32, p33, p35, and p36 are the measurement planes. The position of the radiation source is designated by the arrow.

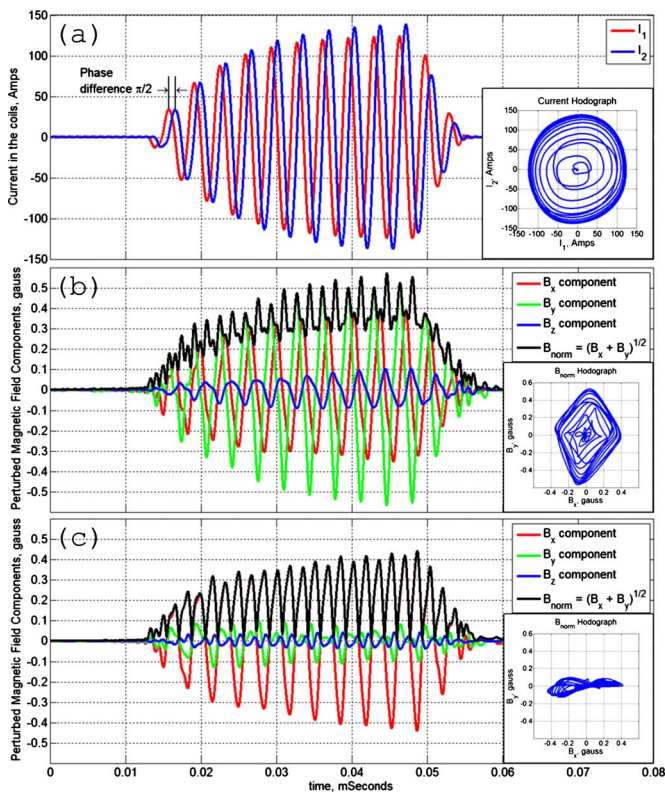


FIG. 4. (Color online) (a) Dependence of input current on time (two currents are on), (b) perturbed magnetic field components on the central line of the machine ~ 86 cm away from the radiation source (two currents are on), and (c) perturbed magnetic field components on the central line of the machine ~ 86 cm away from the radiation source (one current is off).

negligible. First of all the coils are at right angles, thus minimizing the mutual inductance. Further, the alternating currents in the orthogonal loops are independently adjusted (amplitude and phase) by two independent power supplies and two independent LRC driving circuits. These currents are measured throughout the experiments along with the wave magnetic fields and do not change over a data run. Furthermore, we performed the measurements of the currents in both coils even when one of the power supplies was turned off. In that case when one of the currents was ~ 130 A the second was less than 1 A. That is the effect of mutual inductance which was order of 1%. The direction of rotation of the magnetic field created by the antenna can be changed by adjusting the relative phase of the currents in the loops. A driving frequency ($f_d = 293$ kHz) was used so that $\Omega_{ce} \ll \omega \ll \Omega_{ci} \ll \omega_{pe}$.

A typical input signal is shown in Fig. 4(a). The magnetic field components measured at the central axis of the machine at distance ~ 86 cm away from the antenna when both coils were driven with a phase difference $\pi/2$ to generate the RMF are shown in Fig. 4(b). Figure 4(c) shows the output signal when the loop lying in x - z plane was turned off. Two nearly identical currents with peak magnitude ~ 130 A were driven in the loops. In order to create right-handed or left-handed rotation of the magnetic field with respect to the ambient magnetic field direction the relative phase difference was set either $\pi/2$ or $-\pi/2$. To compare the plasma response to the RMF with that of a one-loop antenna,

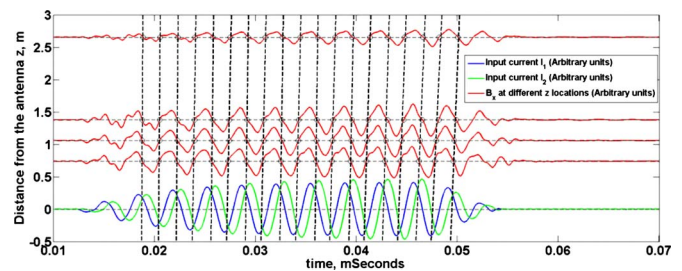


FIG. 5. (Color online) An illustration how the longitudinal phase velocity is determined from the experiment measurements. Red lines represent B_x components of the perturbed magnetic field on the central axis of the LAPD machine at different z locations. Black circles represent the points of the equal phases (in this case zeroes of B_x) in different z locations. Inclined dashed lines are linear fit of the equal phases points, whose slope gives the phase velocity. The input currents are shown for a reference.

experiments were performed with one current turned off. In both cases of the one-loop and two-loop antennas, the B_z component (along the ambient magnetic field) of perturbed magnetic field was much smaller than the perpendicular component. In the two-loop antenna case we get nearly steady perturbed magnetic field, which rotates around the z -axis clockwise or counterclockwise depending on the polarization of the RMF source. While in the case of one loop-antenna we get oscillations of $B_{norm} = \sqrt{B_x^2 + B_y^2}$, and in this case the wave has nearly plane polarization. These features are shown by the hodographs (insets) in Fig. 4.

Figure 5 illustrates a method that we use to determine the longitudinal phase velocity $v_{p||}$ of the generated wave. In order to find $v_{p||}$ we find the equal phase points of the perturbed magnetic field components at different z locations but with the same x and y coordinates. It is convenient to use as such equal phase points zeroes of the magnetic field components (black circles in Fig. 5). Then we fit these points with linear functions (black dashed inclined lines in Fig. 5), whose slope gives the longitudinal phase velocity, which was found to be $v_{p||} = (7.74 \pm 0.76) \times 10^6$ m/s. That gives the wave numbers along the ambient magnetic field $k_{||} = 0.217 - 0.264$ m $^{-1}$, which does not depend on the direction of rotation of the RMF or if it is one-loop antenna. That corresponds to the longitudinal wavelength $\lambda_{||} = 23.8 - 29.0$ m, which is much larger than the antenna size and is larger than the LAPD machine length.

In Fig. 6 normalized spectra of input [Fig. 6(a)] and response [Fig. 6(b)] are presented. One can see that measured signals contain many harmonics of the main frequency, but with significantly smaller amplitudes. In Fig. 7 the wave structures in the plane perpendicular to the ambient magnetic field line for four different instants separated by $T/4 = \pi/(2\omega)$ are presented. The main feature of the plasma response is a two-vortex structure of the magnetic field, which corresponds to field aligned plasma currents. The distance between their centers is ~ 14 cm, which is ~ 1.5 times diameter of the antenna loops. The measurements show that this distance does not depend on time and the distance from the radiation source along z -axis. It implies that in the plane transverse to the ambient magnetic field the wave has nearly constant characteristics and is well confined by the ambient

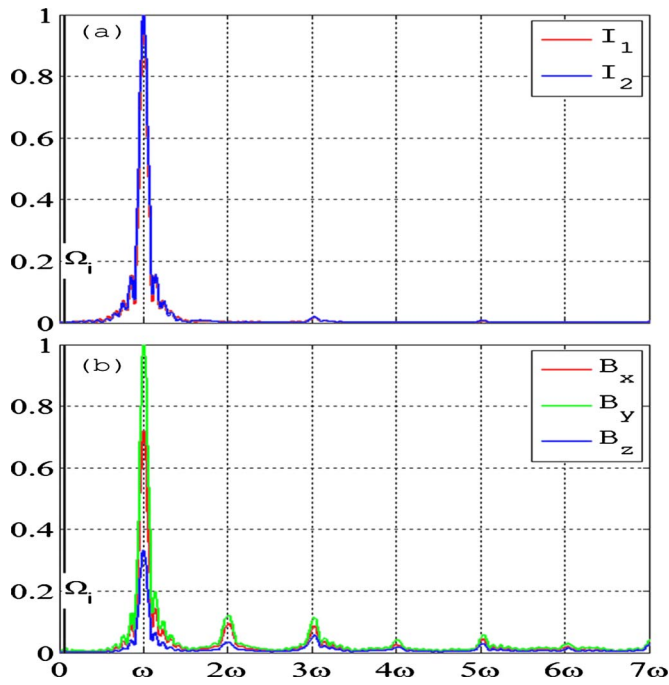


FIG. 6. (Color online) Input current (a) and typical response signal on the central axis of the LAPD machine ~ 86 cm away from the radiation source (b) normalized spectra.

magnetic field. The entire field structure rotates either clockwise or counterclockwise depending on the phase shift between the two input currents. In the one-loop case the radiation pattern does not rotate but oscillates with frequency ω . It means that the circularly polarized whistler wave generated by the RMF source is preferable for creating nonlocal magnetic field gradient than the plane polarized wave generated by the one-loop antenna.

III. COMPARISON OF EMHD MODEL AND EXPERIMENT

A three-dimensional (3D) electron magnetohydrodynamics (EMHD) code described in details in the Appendix was used to simulate the experiment with exactly the same parameters, viz. antenna loops size 9 cm, current magnitude 130 A, driving frequency 293 kHz, electron plasma density $8.3 \times 10^8 \text{ cm}^{-3}$, and ambient magnetic field 50 G. A typical mesh size of $256 \times 256 \times 512$ grid points was used in the simulations. In Fig. 8 the magnetic field structure measured in the experiment [Fig. 8(a)] is compared to the simulations using the 3D EMHD model for the experimental parameters [Fig. 8(b)]. This figure shows the field at the plane perpendicular to the ambient magnetic field for the same instant of time. One can see not only a qualitative but also a quantitative agreement between the 3D EMHD model and the ex-

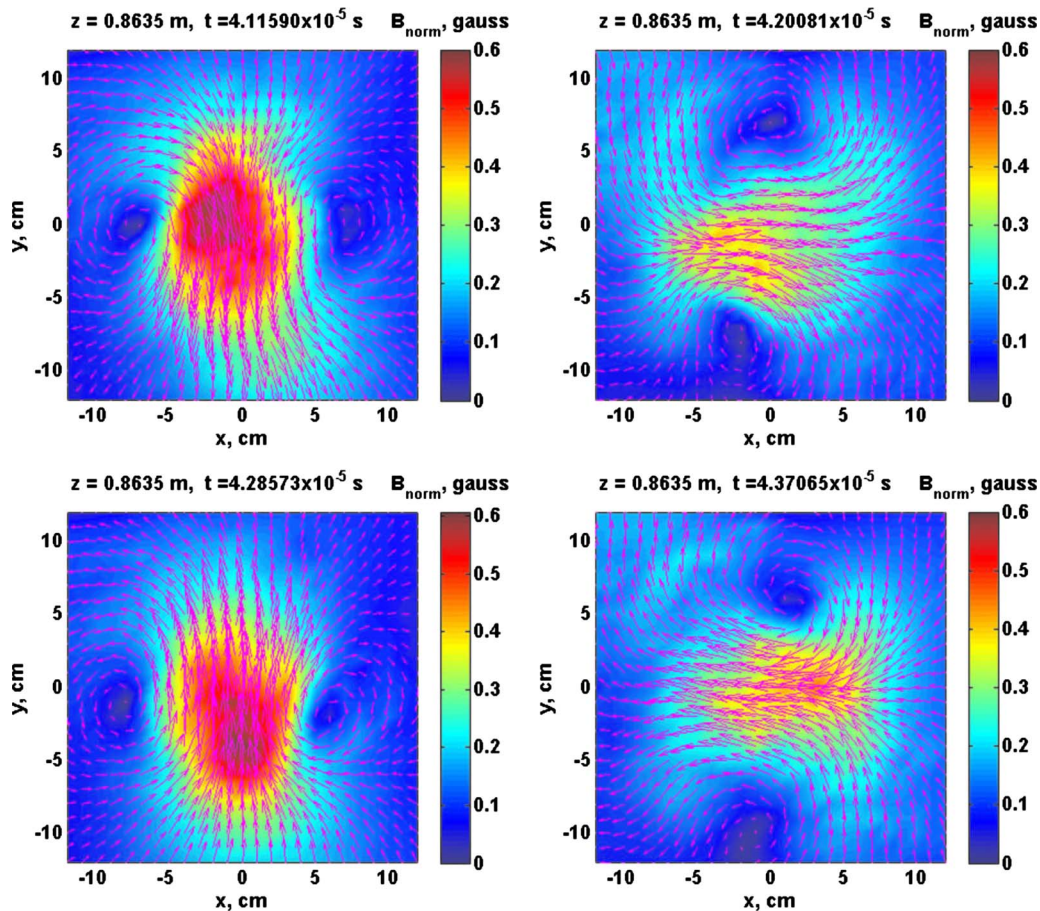


FIG. 7. (Color online) Magnetic field structure at the plane perpendicular to the ambient magnetic field lines at the distance $z=86.35$ cm from the radiation source for four different instants of time separated by one quarter of the period (B_{norm} is the normal to the ambient magnetic field component of perturbed magnetic field).

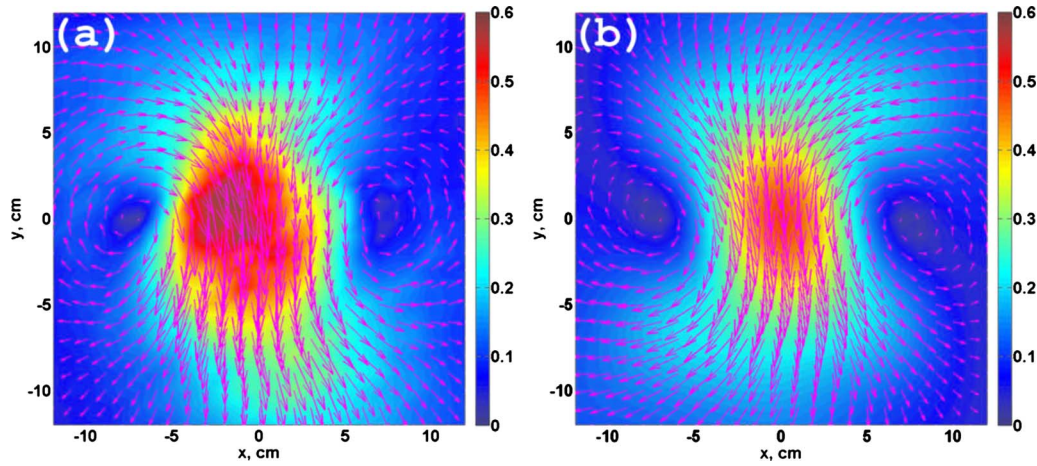


FIG. 8. (Color online) Magnetic field structure in the plane perpendicular to the ambient magnetic field lines at the distance $z=86.35$ cm from the radiation source for some instant of time: (a) measured in the experiment and (b) 3D linear EMHD calculations. (Color palette shows the magnitude of B_{\perp} —normal to the ambient magnetic field component of perturbed magnetic field in gauss.)

periment. Once again we want to draw attention to the two vortex structures of the magnetic field corresponding to the field aligned plasma currents.

The radiation patterns (square of the normal component of the magnetic field averaged over a period of rotation, which is essentially the wave intensity) for one-loop (Fig. 9)

and two-loop with right handed rotation (Fig. 10) cases measured in experiments (a.1)–(a.4) and calculated using the 3D EMHD models (b.1)–(b.4) are presented. Also in Figs. 9 and 10 the comparison of experimental and model dependence of the magnitude of the perturbation along the transverse coordinates (c.1)–(c.4) are presented. One can see good overall

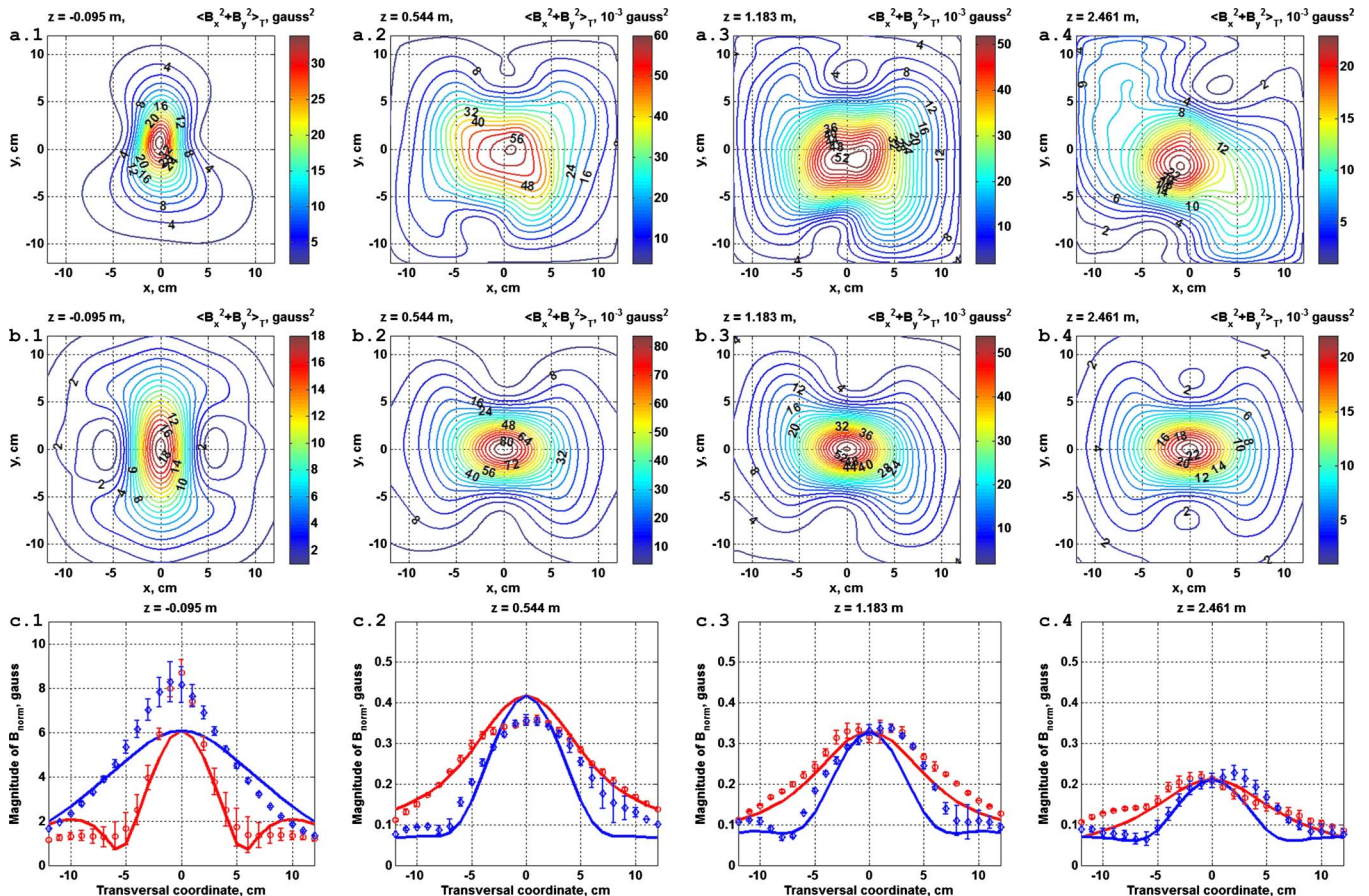


FIG. 9. (Color online) Radiation pattern ($\langle B_x^2+B_y^2 \rangle_T$) averaged over a period $T=1/f_D$, that is wave intensity up to some coefficient) for one loop case (loop lying in yz plane is turned on). (a.1)–(a.4) Experimental measurements, (b.1)–(b.4) 3D EMHD model, and (c.1)–(c.4) comparison of experimental and EMHD calculated dependencies of the magnitude of normal component of perturbed magnetic field along transverse axes (dots—experimental measurements, solid lines—EMHD model, red—cross section in x direction, blue—cross section in z direction).

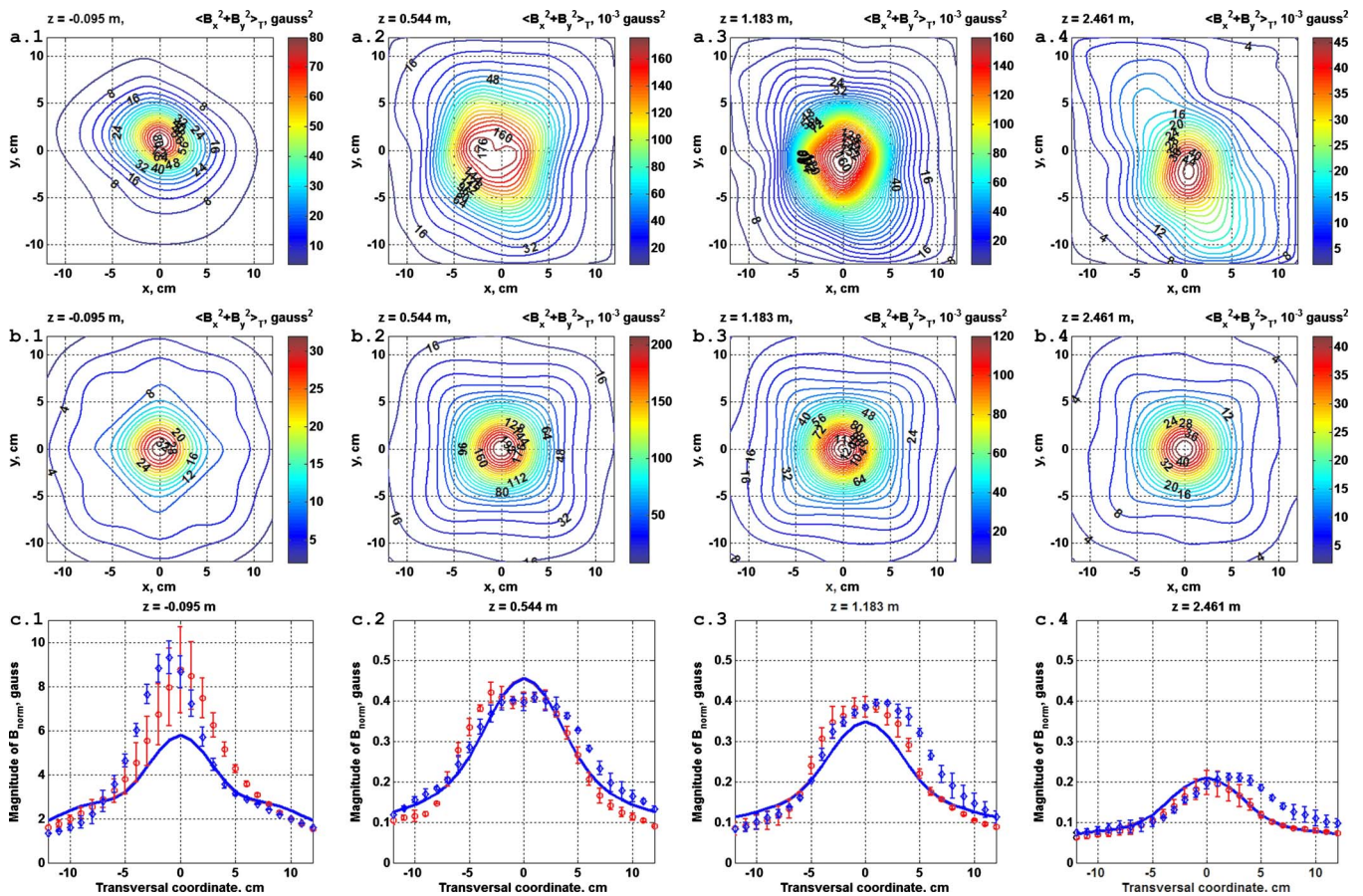


FIG. 10. (Color online) Radiation pattern ($\langle B_x^2 + B_y^2 \rangle_T$) averaged over a period $T=1/f_D$, that is wave intensity up to some coefficient) for two loop case (right handed rotation of the RMF). (a.1)–(a.4) Experimental measurements, (b.1)–(b.4) 3D EMHD model, and (c.1)–(c.4) comparison of experimental and EMHD calculated dependencies of the magnitude of normal component of perturbed magnetic field along transverse axes (dots—experimental measurements, solid lines—EMHD model, red—cross section in x direction, blue—cross section in z direction).

agreement of the experimental results and calculated using the 3D EMHD model for both one-loop and two-loop antenna cases. The main feature of the radiation pattern for both cases is that the characteristic size of the spot in the direction transverse to the ambient magnetic field does not depend on the distance from the antenna along the field line, while the magnitude of the magnetic field perpendicular to the ambient magnetic field decreases due to energy leakage away from it and due to the effect of collisions, which will be discussed further.

In Fig. 11 the dependence of the magnitude of the normal to the ambient magnetic field component of perturbed magnetic field calculated using EMHD model, described in the Appendix, on distance from the antenna along the z -axis is compared with the experiment (a) and fitting functions (b). The best agreement between the EMHD calculations and experimental measurements were obtained for the effective collision frequency $\nu=0.007\Omega_{ce}\approx 6.2\times 10^6\text{ s}^{-1}$. Also in Figs. 11(a) and 11(b) the dependence of the magnitude of perturbed magnetic field for the nondissipative case is presented. For the nondissipative case we fitted the magnitude dependence on distance from the source z for $z>0.5\text{ m}$. It

was found that the magnitude depends on z as $\sim 1/\ln(az+b)$ which is actually a very slow decay rate compared, for example, with $1/z$. This slow decay rate distinguishes the generation of the whistler waves by magnetic dipole and the RMF source antennas from the generation of whistler waves by an electric dipole antenna, which has been studied by many authors theoretically, experimentally, and numerically.^{12–18} In Ref. 14 it is clearly demonstrated that in the case of linear small magnitude whistler waves driven by the electric dipole antenna the magnitude of the wave decays very fast along the ambient magnetic field even in the collisionless plasma due to the fact that the energy radiated is nearly evenly distributed inside the resonance cone. In order to force the self-ducting of the whistler waves along the ambient magnetic field it is necessary to drive fairly large magnitude waves, which are able to modify plasma itself due to nonlinear wave-particle interaction. In our case, the whistler waves generated by the magnetic dipole and the RMF antennas the perturbation is weak compared to the ambient magnetic field, more over, the model described in the Appendix is purely linear, and the plasma density is uniform, but still we are able to generate the wave in which almost all the energy transfers along the ambient magnetic field and only a

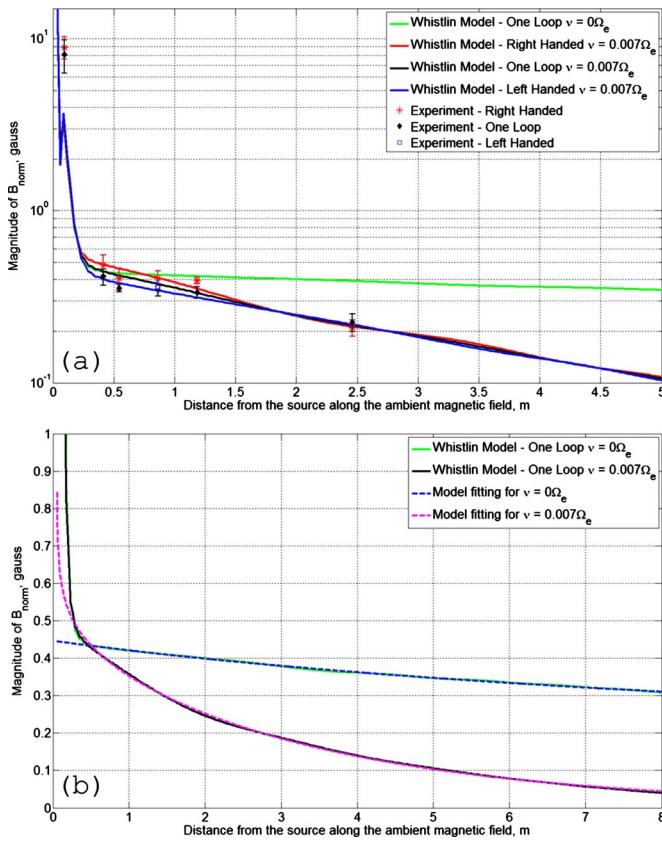


FIG. 11. (Color online) Dependence of the magnitude of normal to the ambient magnetic field component of perturbed magnetic field along the ambient magnetic field: (a) comparison of EMHD model with the experiment, (b) fitting of the EMHD model results by a functions $\sim 1/\ln(az+b)$ for collisionless case ($\nu=0$), and $\sim \exp(-z/d)/\ln(az+b)$ for case with collisions ($\nu=0.007\Omega_{ce}$).

small portion of it goes to peripheral, which determines the slow decay rate. This is possible because of significant field aligned plasma currents. This feature becomes more important for the circularly polarized whistler wave generated by the RMF source. It means that we are able to create a perturbation of the magnetic field, whose value never goes to zero, over a very long distance in space plasma, which is essentially collisionless. For the dissipative case with effective collision frequency $\nu=0.007\Omega_{ce}$ the best fit is with function $\sim \exp(-z/d)/\ln(az+b)$ with characteristic decay distance $d=3.704$ m.

Although the overall agreement between the experimental measurements and EMHD model results is good, the difference at the plane closest to antenna (9.5 cm) is significant. At this location the model yields magnitudes, which are nearly half of the experimental values. The reason for this is the way the simulation code is implemented. As one can see from Fig. 11 in the region close to the antenna the magnitude

decays very fast from ~ 10 to ~ 0.5 G at 10 cm distance, and its spectrum has very high harmonics. However in our calculations we are forced to reduce the number of harmonics in the Fourier domain, which are determined by the grid size.

Using parameters of the experiment such as gas pressure, temperature of neutrals, electrons, and ions and plasma density, we can estimate effective electron-neutral ν_{en} and electron-ion ν_{ei} collision frequencies. For electron-neutral collision frequency empirical formula from Ref. 19 gives $\nu_{en} \approx 5.6 \times 10^4 \text{ s}^{-1}$, which is two orders of magnitude lower than the collision frequency in the model. For electron-ion collision frequency the estimate²⁰ is $\nu_{ei} \approx 5.8 \times 10^6 \text{ s}^{-1}$, which is very close to the value $\nu=0.007\Omega_{ce} \approx 6.2 \times 10^6 \text{ s}^{-1}$ obtained from EMHD model for the best match with the experimental measurements. This implies that, the whistler wave generation experiment along with presented 3D EMHD model could be used to estimate the electron collision frequency.

Now we want to discuss the properties of the whistler wave dispersion relation. For the experimental parameters the plasma $\beta = nk_B T / (B_0^2 / 2\mu_0) \sim 10^{-3} \ll 1$ and cold magneto-hydrodynamics approach is applicable. The general dispersion relation in the frames of MHD approach could be written as⁵

$$\tan^2 \theta = \frac{n_{\perp}^2}{n_{\parallel}^2} = - \frac{P(n^2 - R)(n^2 - L)}{(Sn^2 - RL)(n^2 - P)}, \quad (2)$$

where θ is the angle between the direction of the ambient magnetic field \mathbf{B}_0 and wave vector \mathbf{k} , $\mathbf{n} = c\mathbf{k}/\omega$, $n_{\perp} = ck_{\perp}/\omega$, and $n_{\parallel} = ck_{\parallel}/\omega$, where k_{\perp} and k_{\parallel} are the components of the wave number normal and parallel to the ambient magnetic field ($k_{\perp} = k \sin \theta$, $k_{\parallel} = k \cos \theta$). The terms R , L , P , and S are given by

$$R = 1 - \sum_s \frac{\omega_{ps}^2}{\omega^2} \frac{\omega}{\omega + i\nu_s + \Omega_{cs}}, \quad (3)$$

$$L = 1 - \sum_s \frac{\omega_{ps}^2}{\omega^2} \frac{\omega}{\omega + i\nu_s - \Omega_{cs}}, \quad (4)$$

$$P = 1 - \sum_s \frac{\omega_{ps}^2}{\omega^2} \frac{\omega}{\omega + i\nu_s}, \quad (5)$$

$$S = \frac{R + L}{2}, \quad (6)$$

where s denotes sum over all species (electrons and helium ions in our case), ω_{ps} , Ω_{cs} , and ν_s are the plasma, cyclotron, and effective collision frequencies of the specie s , respectively. Resolving Eq. (2) with respect to n^2 we get

$$n_{1,2}^2 = \frac{[PS(1 + \cos^2 \theta) + RL \sin^2 \theta] \pm \sqrt{(PS - RL)^2 \sin^4 \theta + P^2(R - L)^2 \cos^2 \theta}}{2(S \sin^2 \theta + P \cos^2 \theta)} \quad (7)$$

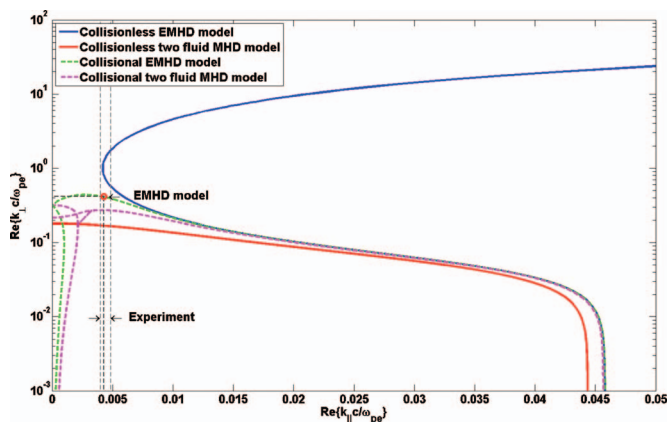


FIG. 12. (Color) Relation of the transverse wave number k_{\perp} to the longitudinal wave number k_{\parallel} for the whistler wave with frequency $\omega = 0.002\,093\Omega_{ce}$ (used in the experiment).

as a function of the wave vector direction. Setting the parameters used in the experiment, we get the relation between the longitudinal wave number k_{\parallel} and the transverse wave number k_{\perp} (see Fig. 12).

First, we consider collisionless plasma case ($\nu_s=0$). In the EMHD model we neglect the ion motion. In this limit the dispersion relation [Eq. (2)] reduces to the quasilongitudinal whistler wave dispersion relation [Eq. (A22)]. The EMHD model relation is represented by blue solid line in Fig. 12. The presence of ion motion modifies the whistler wave refraction index surface. Particularly, for the experimental frequency $\omega = 0.002\,093\Omega_{ce}$ the relation between the longitudinal k_{\parallel} and transverse k_{\perp} wave numbers behaves fundamentally differently (red solid line in Fig. 12). For the experimental frequency in the two fluid MHD model the transverse wave number k_{\perp} has a cutoff above which the whistler wave mode is evanescent, unlike the EMHD model refractive index surface which is unbounded. It was shown^{21,22} that the frequency, which separates this two regimes, is the lower-hybrid resonance $\omega_{LH} = \sqrt{\Omega_{ci}\Omega_{ce}} = 1.03 \times 10^7 \text{ s}^{-1}$. Moreover, the EMHD model is applicable to the collisionless cold plasma only if the driving frequency ω is well above the lower hybrid resonance ω_{LH} .²² In our case the experimental driving frequency ω lies below the ω_{LH} , and, in general, the EMHD approach is not applicable to describe our experiment. However, the inclusion of the finite effective collision frequencies ν_s in Eq. (2) changes the picture.

We estimated the collision frequencies for electrons to be $\nu_{en} \approx 5.6 \times 10^4 \text{ s}^{-1}$ (electron-neutral collisions) and $\nu_{ei} \approx 5.8 \times 10^6 \text{ s}^{-1}$ (electron-ion collisions). The experimental parameters yield the ion-neutral collision frequency order of 10^2 s^{-1} . Thus, for both species, electrons and ions, the collisions are dominated by the Coulomb collisions. Strictly speaking, the dispersion relation [Eq. (2)] is not valid in that case because of the momenta exchange between the two species, and more accurate expressions should be used, but to a first approximation the effect of ion-electron collisions in the two fluid MHD model could be included by using as the effective ion collisions rate the value $\nu_i = (m_e/m_i)\nu_{ei}$ in Eq. (2).²³ Using this value of the collision frequencies we get the relations of the real parts of longitudinal and transverse wave

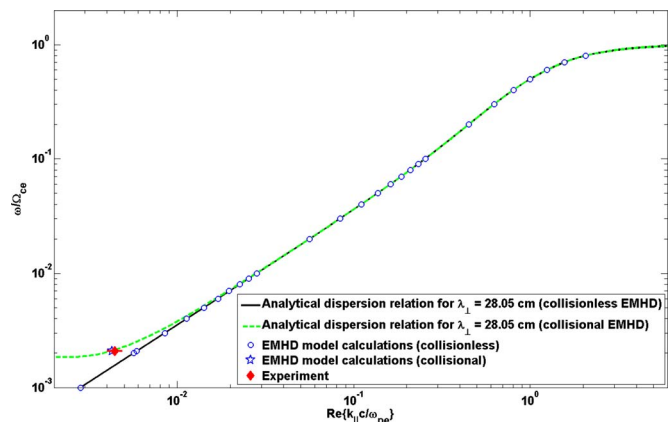


FIG. 13. (Color online) Comparison of analytical dispersion relation, EMHD model calculations, and the experiment for $\lambda_{\perp} = 28.05 \text{ cm}$.

numbers in the EMHD (green dashed line in Fig. 12) and two fluid MHD (magenta dashed line in Fig. 12) models. One can see that below a certain transverse wave number the dispersion relations from all three models, viz. the collisionless EMHD, collisional EMHD, and collisional two fluid MHD, essentially yield the same mode. From the simulations we found the longitudinal wave number to be $k_{\parallel} = 0.2312 \text{ m}^{-1}$ ($\lambda_{\parallel} = 27.18 \text{ m}$). That corresponds to the transverse wave number $k_{\perp} = 22.40 \text{ m}^{-1}$ ($\lambda_{\perp} = 28.05 \text{ cm}$) on the collisional EMHD dependence (red circle in Fig. 12). This transverse wavelength is two times the distance between the vortices in the field structure corresponding to the field aligned currents. This result does not depend on driving frequency ω or the distance from the antenna along the ambient magnetic field, but is determined by the size of the antenna. We did a series of simulations using 3D EMHD model varying the diameter of the antenna loops, and it was found that the distance between the vortices in the magnetic field structure (that is half of transverse wavelength $\lambda_{\perp}/2$) is roughly the size of antenna, within a couple of electron skin depths. Again we emphasize here that the distance between two vortices in the wave picture corresponding to the field aligned plasma currents does not depend on the distance from the antenna along the ambient magnetic field. The range of experimentally measured longitudinal wavelength $\lambda_{\parallel} = 23.8\text{--}29.0 \text{ m}$ corresponds to the transverse wavelength $\lambda_{\perp} \approx 42 \text{ cm}$ in the frames of two fluid MHD model, which is 1.5 times larger than the value in the frames of the EMHD model.

In Fig. 13 the dispersion relation for $\lambda_{\perp} = 28.05 \text{ cm}$ is presented. The solid black line represents the analytical dispersion relation [Eq. (A24)] in the collisionless limit. The green dashed line represent analytical dispersion relation in the frames of EMHD model taking into account the finite collision frequency $\nu_e = 0.007\Omega_{ce}$. Results of the 3D EMHD modeling (blue circles and blue pentagram) lie on top of the theoretical curves. The experimental point (red diamond) is also in good agreement with the analytical dispersion relation.

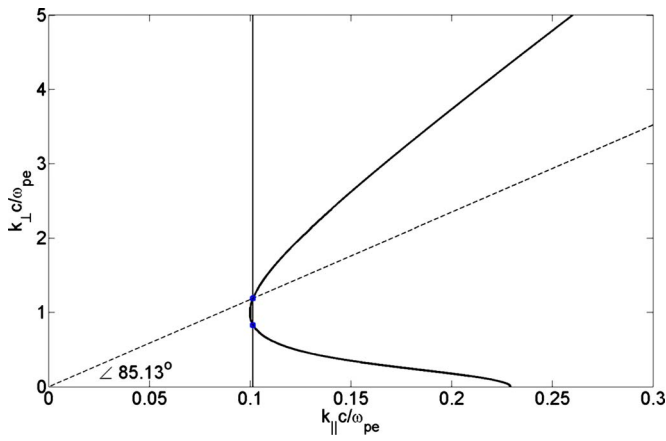


FIG. 14. (Color online) Dependence of the transverse wave number k_{\perp} on the longitudinal wave number k_{\parallel} for frequency $\omega=0.05\Omega_{ce}$.

IV. WAVE STRUCTURE FROM THE DISPERSION RELATION

Finally we present some general properties of the dispersion relation [Eq. (A24)] and the corresponding wave structures generated by magnetic loop and RMF antennas in three dimensions. First of all the effect of finite transverse wave number k_{\perp} makes the dispersion relation [Eq. (A24)] very different from the dispersion relation [Eq. (A23)] for the plane whistler wave propagating along ambient magnetic field with zero k_{\perp} , which is well known. For example, in the three dimensional case, whistler waves generated by a finite size antenna can have a polarization different from the plane whistler wave with zero k_{\perp} , which is right hand polarized.

In Fig. 14 the dependence of k_{\perp} on k_{\parallel} given by Eq. (A24) for frequency $\omega=0.05\Omega_{ce}$ is presented. The main feature of the dependence is that above the value ~ 0.1 and below ~ 0.225 for every k_{\parallel} there are two corresponding values of k_{\perp} . That is for the same k_{\parallel} , two waves with different k_{\perp} can be generated. The vertical solid line in Fig. 14 represents the longitudinal wave number k_{\parallel} found using the 3D EMHD model for the frequency $\omega=0.05\Omega_{ce}$ and the current loop diameter $\sim 4.9d_e$. For this longitudinal wave number k_{\parallel} there are two corresponding transverse wave numbers (blue circles). The lowest of them corresponds to the distance ~ 14.0 cm between the centers of two vortices in the magnetic field structure (see Figs. 7 and 8) corresponding to the field aligned plasma currents.

The relationship of k_{\parallel} to k_{\perp} determines the direction of the wave vector \mathbf{k} , which is the direction of the phase velocity. The angle between this wave vector \mathbf{k} and the z -axis is 85.13° and corresponding wave front has slope 4.87° with respect to the z -axis. In Fig. 15 the dependence of the B_x component (perpendicular to the plane of the picture) of perturbed magnetic field in the plane containing the current loop for the driving frequency $\omega=0.05\Omega_{ce}$ is presented. One can see the two wave structures of the whistler wave excited by the finite size antenna. Both waves share the same longitudinal wave number k_{\parallel} , but they have different transverse wave numbers k_{\perp} determined by the dispersion relation [Eq. (A24)]. The wave vector corresponding to higher transverse

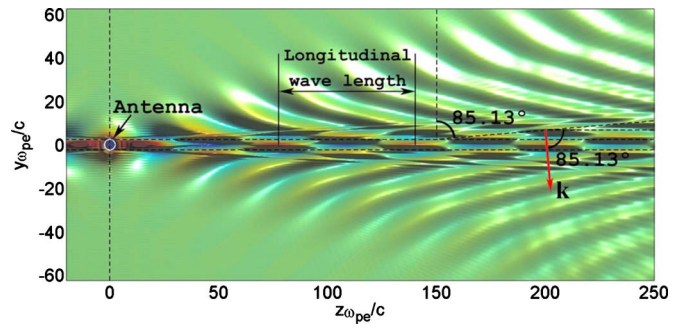


FIG. 15. (Color online) B_x component (perpendicular to the plane of the picture) of the perturbed magnetic field in the plane containing the loop with the current (ring at the origin) for the frequency $\omega=0.05\Omega_{ce}$.

wave number k_{\perp} is shown. It has angle 85.13° with respect to the z -axis.

In Fig. 16 the plasma current structure in the plane containing the loop with the current corresponding to the wave shown in Fig. 15 is presented. The color shows the J_x component of the plasma current and the black curves represent plasma current flow-lines in the plane of the picture. Again one can see the two wave structure of the excited whistler wave in the plasma current structure. We should furthermore emphasize that in Fig. 16 the dominant plasma current is concentrated near the z -axis, and the width of the current loops on the symmetry axis does not change with the distance from the antenna. The plasma current forms a chainlike structure whose characteristic size (that is the transverse wavelength) is determined by the size of the antenna and does not depend on distance from the antenna along the ambient magnetic field line. The maxima of the field aligned current correspond to the centers of the vortices in the magnetic field structure in the plane perpendicular to the ambient magnetic field. The length of the “chain segments” is determined by the dispersion relation [Eq. (A24)] and become longer when the driving frequency ω goes down. In the case of the two-loop antenna generating the RMF this chain structure has right or left handed helicity depending on the phase difference in the antenna currents. So the major part of the

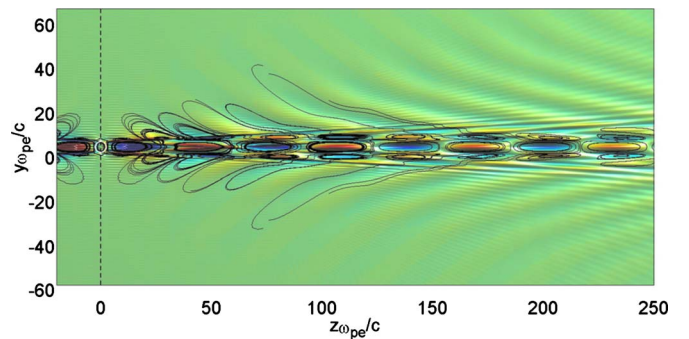


FIG. 16. (Color online) Plasma current structure in the plane containing the loop with the current (ring in the origin) for the frequency $\omega=0.05\Omega_{ce}$. Color shows J_x component (perpendicular to the plane of the picture) of the current. The black curve lines represent plasma current flow lines in the plane of the picture. (The current flow lines only for the region close to the symmetry axis are shown.)

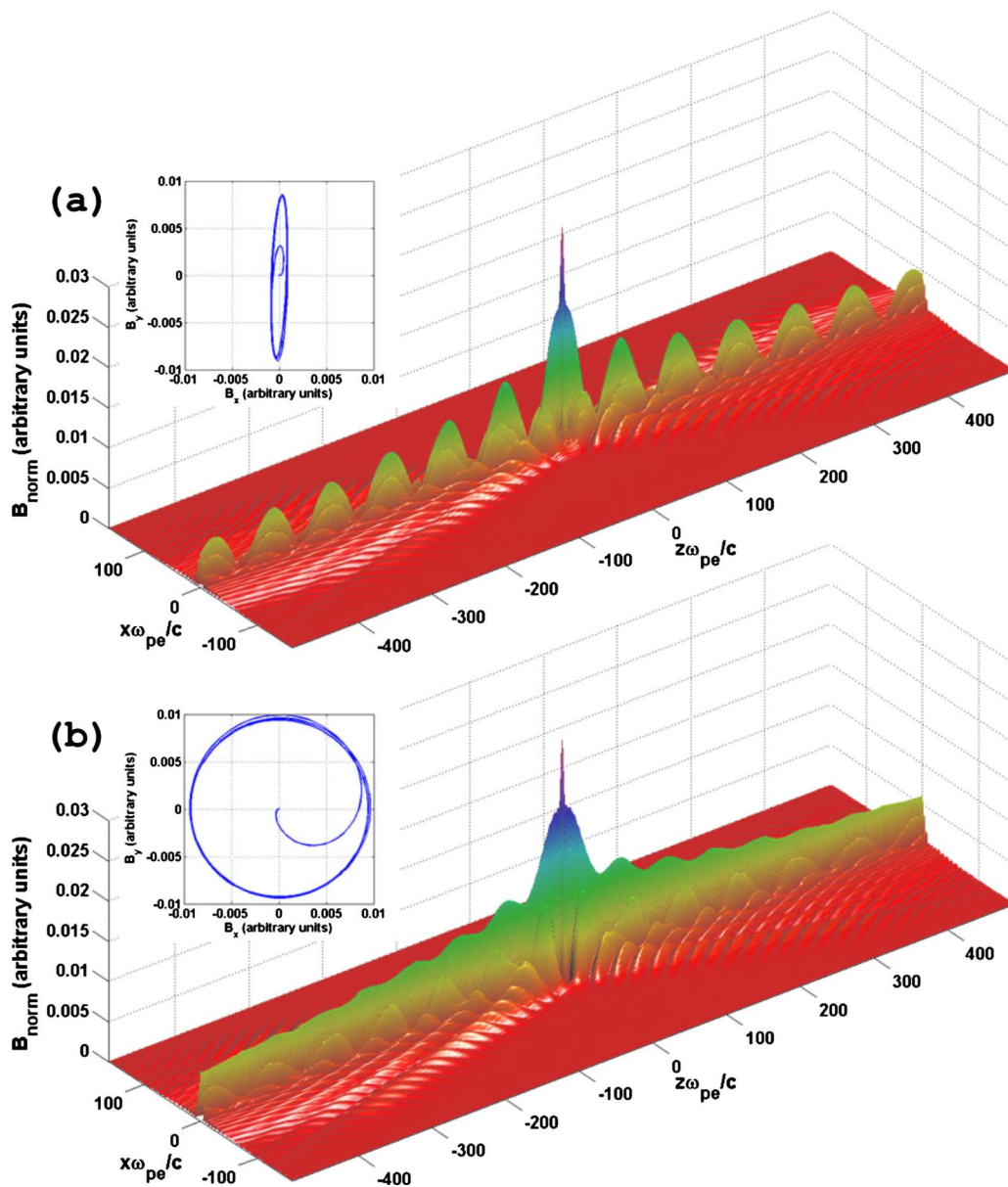


FIG. 17. (Color online) Distribution of the normal component of the wave magnetic field for some instance of time generated by one-loop (a) and two-loop antenna with right-handed polarization (b). The one loop antenna lays in xz plane at the origin. The loops of two-loop antenna lay in xz and xy planes at the origin. (Antenna loop diameter ~ 4.9 electron skin depth, driving frequency $\omega = \Omega_{ce}/50$, collisionless case.)

plasma current is field aligned and well confined by the ambient magnetic field. It explains the very slow decay rate of the whistler waves generated by the magnetic dipole and the two-loop antennas.

Finally, we want to discuss the difference between the whistler waves generated by the one-loop antenna and the two-loop RMF source. In Fig. 17 a distribution of the perturbed magnetic field component B_{norm} normal to the ambient magnetic field for some instance of time in the whistler wave driven in collisionless plasma with frequency $\omega = \Omega_{ce}/50$ by one-loop [Fig. 17(a)] and two-loop [Fig. 17(b)] antennas is presented. The insets feature the polarization of the wave in the central symmetry axis. In one-loop antenna case the polarization is right-handed elliptical, and nearly plane. For two-loop antenna case the wave is right-handed

(or left-handed, depending on the phase difference of the driving currents) circularly polarized. The ellipticity in one-loop case depends on the driving frequency ω . For low frequencies $\omega \ll \Omega_{ce}$ the ellipticity is nearly 1, and the waves generated by the one-loop antenna have nearly plane polarization. It is consistent with the experiment [see inset on Fig. 4(c)]. When the frequency goes up and approaches $\omega = 0.5\Omega_{ce}$ the polarization of the wave generated by one-loop antenna become more circular. One can see that in both cases of one-loop and two-loop RMF antennas the wave front is very narrow corresponding to the antenna size and decays slowly along z -direction due to peripheral leakage of energy. From the simulations we estimate the amount of the wave energy inside the central channel within the radius of $\lambda_{\perp}/2$ relative to the all energy radiated as

$$\epsilon(z) = \frac{\int_0^{\lambda_{\perp}/2} \rho B_{\text{norm}}^2(\rho, z) d\rho}{\int_0^{\infty} \rho B_{\text{norm}}^2(\rho, z) d\rho}, \quad (8)$$

where B_{norm} is the magnitude of the normal component of the wave field. We found that wave energy which stays within the $\lambda_{\perp}/2$ radius is order of 75%–85% (depending on the driving frequency) of the whole energy radiated. It means that the magnetic dipole and RMF source antennas are very efficient for transferring radiation along the ambient magnetic field. The other feature that distinguishes one-loop antenna from the two-loop antenna case is that in two-loop antenna case the normal component of the perturbed magnetic field is sufficiently nonzero along the central symmetry axis while in the one-loop antenna case it oscillates in space. That is consistent with the experiment (see Fig. 4). This feature is important for generation of nonlocal field gradient and nonresonant scattering of energetic particles.

V. CONCLUSION

We have demonstrated the concepts of a new type the RMF-based antenna/active device for generation whistler waves. We investigated the interactions of the RMF (for the frequency $\Omega_{ci} \ll \omega \ll \Omega_{ce} \ll \omega_{pe}$) with magnetized plasma in experiments and three-dimensional EMHD simulations. We found very good agreement of the linear 3D EMHD model with the experiment, not only qualitatively, but also quantitatively. We found that the whistler waves generated by both the one-loop and two-loop antennas are confined by the ambient magnetic field without nonlinear wave particle interaction and/or plasma density ducts. The generated wave structures has significant field aligned plasma currents confined by the ambient magnetic field. That allows to transfer the radiation along the ambient magnetic field very efficiently. In the collisional plasma the wave decay rate is determined by Coulomb collisions. In the collisionless case very slow decay rate is determined by the leakage of the wave energy from the central axis to peripheral. The whistler wave generated by the RMF has sufficiently nonzero normal component along the central symmetry axis while in the one-loop antenna case the normal component of the wave magnetic field oscillates along the ambient magnetic field. Analytical dispersion relation for whistler wave in cold plasma, Eq. (A24), is in very good agreement with the results of the 3D EMHD simulations and the experimental measurements. The whistler wave generation by magnetic dipole along with the 3D EMHD model is used for estimating an effective electron collision frequency.

ACKNOWLEDGMENTS

The work was supported by ONR MURI Grant No. N000140710789. The experiments were done on the LAPD at UCLA. The device is a part of the Basic Plasma Science Facility funded by the Department of Energy (Contract No. DE-FC02-07ER54918) and the National Science Foundation (Contract No. NSF-PHY-0531621).

APPENDIX: LINEAR MODEL OF WHISTLER WAVE PROPAGATION

Here we describe a linear model which was used to simulate the propagation of whistler waves generated by a RMF using a 3D linear spectral code. Following the EMHD approach,^{18,24–26} starting from the Maxwell and the electron momentum equations, neglecting the displacement current and assuming stationary ions (for the frequency range $\Omega_{ci} \ll \omega \ll \Omega_{ce}$), the equations governing a quasineutral cold electron fluid can be written as

$$\nabla \times \mathbf{E} = -\frac{1}{c} \frac{\partial \mathbf{B}}{\partial t}, \quad (A1a)$$

$$\nabla \times \mathbf{B} = -\frac{4\pi}{c} en\mathbf{v} + \frac{4\pi}{c} \mathbf{J}_{\text{ext}}, \quad (A1b)$$

$$\frac{\partial \mathbf{v}}{\partial t} + (\mathbf{v} \cdot \nabla) \mathbf{v} = -\frac{e}{m_e} \mathbf{E} - \frac{e}{m_e c} \mathbf{v} \times \mathbf{B} - \nu \mathbf{v}, \quad (A1c)$$

where \mathbf{E} and \mathbf{B} are electric and magnetic fields, \mathbf{v} is the velocity of the cold electron fluid, $n = n_0(\mathbf{x})$ is the number plasma density, which is space dependent, but assumed to be independent on time, e and m_e are the electron charge and mass, \mathbf{J}_{ext} is an external current density, and ν is an effective frequency of electron collisions either with ions or neutrals. We further consider a simplified case of uniform electron plasma $n(\mathbf{x}) = n_0 = \text{const}$. We also consider a case of uniform background magnetic field, i.e., $\mathbf{B} = \mathbf{B}_0 + \mathbf{B}'$, where \mathbf{B}_0 is a constant in time and space and \mathbf{B}' is a magnetic field perturbation.

Normalizing length by the electron skin depth $L = c/\omega_{pe}$ and time by the inverse of the electron cyclotron frequency $T = \Omega_e^{-1}$, the normalized variables become $\bar{t} = t/T$, $\bar{\mathbf{x}} = \mathbf{x}/L$, $\bar{\mathbf{v}} = T\mathbf{v}/L$, $\bar{\mathbf{B}} = \mathbf{B}/B_0$, $\bar{\mathbf{E}} = (cT\mathbf{E})/(LB_0)$, and $\bar{\nu} = \nu/\Omega_{ce}$. We can then rewrite Eq. (A1) in the linearized form,

$$\bar{\nabla} \times \bar{\mathbf{E}} = -\frac{\partial \bar{\mathbf{B}}}{\partial \bar{t}}, \quad (A2a)$$

$$\bar{\nabla} \times \bar{\mathbf{B}} = -\bar{\mathbf{v}} + 4\pi \bar{\mathbf{J}}_{\text{ext}}, \quad (A2b)$$

$$\frac{\partial \bar{\mathbf{v}}}{\partial \bar{t}} = -\bar{\mathbf{E}} - \bar{\mathbf{v}} \times \mathbf{b} - \bar{\nu} \bar{\mathbf{v}}, \quad (A2c)$$

where $\bar{\mathbf{B}}$ is the perturbed magnetic field and \mathbf{b} is the unit vector in the direction of the ambient magnetic field \mathbf{B}_0 , chosen to be along the z -axis. The external current \mathbf{J}_{ext} , which is used to drive the RMF, can be introduced in the model as the loops of the antenna. In our case the size of the antenna is much smaller than the wavelength, and if we want to resolve both the wavelength and the size of the antenna we must use either nonuniform or very fine mesh with a large number of cells. Instead of this we use an analytic solution which removes the necessity to resolve the antenna size by mesh. From this point to the end we will work only with dimensionless variables, so we drop the bars in the remaining section of the paper. We decompose the electric and magnetic

field perturbations into wave fields and the given localized driving fields ($\mathbf{E}=\mathbf{E}'+\mathbf{E}_{\text{drive}}$, $\mathbf{B}=\mathbf{B}'+\mathbf{B}_{\text{drive}}$) with

$$\mathbf{E}_{\text{drive}} = -\frac{\partial}{\partial t}\mathbf{A}_{\text{drive}}, \quad (\text{A3a})$$

$$\mathbf{B}_{\text{drive}} = \nabla \times \mathbf{A}_{\text{drive}}, \quad (\text{A3b})$$

where $\mathbf{A}_{\text{drive}}$ is a vector potential that satisfies the equation

$$\nabla \times \nabla \times \mathbf{A}_{\text{drive}} + \mathbf{A}_{\text{drive}} = 4\pi\mathbf{J}_{\text{ext}}. \quad (\text{A4})$$

Solution of Eq. (A4) can be written in terms of a Green's function as

$$\mathbf{A}_{\text{drive}}(\mathbf{r}, t) = \int_C \mathbf{J}_{\text{ext}}(\mathbf{r}', t) G(\mathbf{r}, \mathbf{r}') dC(\mathbf{r}'), \quad (\text{A5})$$

where C is the current contour and $G(\mathbf{r}, \mathbf{r}')$ is the Green's function,

$$G(\mathbf{r}, \mathbf{r}') = \frac{1}{|\mathbf{r} - \mathbf{r}'|} \exp(-|\mathbf{r} - \mathbf{r}'|). \quad (\text{A6})$$

The principle of superposition is applicable to the vector potential $\mathbf{A}_{\text{drive}}$ and it can be calculated for each current independently. In Eq. (A5) the time dependence appears only as $\exp(-i\omega t)$, thus the value of $\mathbf{A}_{\text{drive}}$ should be calculated only once at the very first time step.

Using Eqs. (A3) and (A4), Eq. (A2) can be written as

$$\frac{\partial \mathbf{v}}{\partial t} = \nabla \times \nabla \times \mathbf{E}' + \frac{\partial}{\partial t}\mathbf{A}_{\text{drive}}, \quad (\text{A7a})$$

$$\nabla \times \mathbf{B}' = -\mathbf{v} + \mathbf{A}_{\text{drive}}, \quad (\text{A7b})$$

$$\nabla \times \nabla \times \mathbf{E}' + \mathbf{E}' = -\mathbf{v} \times \mathbf{b} - \nu \mathbf{v}. \quad (\text{A7c})$$

Equation (A7) can be solved numerically using a special method in three dimensions, noting that the time dependence enters only in Eq. (A7a). We can construct the algorithm for numerical integration of the system in the following way. For given \mathbf{E} , \mathbf{B} , and \mathbf{v} at $t=t_n$, using Eq. (A7a), we can perform one step integration in time to get \mathbf{v} at instant $t=t_{n+1}$. This new value of \mathbf{v} is used to obtain \mathbf{B} and \mathbf{E} at $t=t_{n+1}$, and the process is repeated. This approach to the solution of Eq. (A7) was used in Refs. 18 and 26. The advantage of this method is that this algorithm can handle the fully nonlinear problem [Eq. (A1)] without dropping the convective term $(\nabla \cdot \mathbf{v})\mathbf{v}$ and the nonlinear $\mathbf{v} \times \mathbf{B}'$ term. The problem with this method when using the spectral method is that we have to resolve Eq. (A7) for every possible Fourier component \mathbf{k} . Since the time step should be small enough to resolve the electron cyclotron frequency we have to perform many thousands of steps to resolve at least one period of oscillation for the case when the driving frequency $\omega \ll \Omega_{ce}$. Besides in the present work we consider only the linear case of whistler waves for which an analytical solution of Eq. (A7) can be obtained.

We select the reference frame in such a way that the ambient magnetic field \mathbf{B}_0 is oriented along the z -axis ($\mathbf{b} = \mathbf{e}_z$). In the Fourier domain from Eq. (A7) we get the electric field \mathbf{E}^* expressed through the velocity \mathbf{v}^* ,

$$\mathbf{E}^* = -\frac{\mathbf{v}^* \times \mathbf{e}_z + \nu \mathbf{v}^* + \mathbf{k}[\mathbf{k} \cdot (\mathbf{v}^* \times \mathbf{e}_z)]}{1 + k^2}, \quad (\text{A8})$$

and the closed system for the velocity \mathbf{v}^* ,

$$\frac{\partial \mathbf{v}^*}{\partial t} = \frac{-k^2(\mathbf{v}^* \times \mathbf{e}_z + \nu \mathbf{v}^*) + \mathbf{k}[\mathbf{k} \cdot (\mathbf{v}^* \times \mathbf{e}_z)]}{1 + k^2} + \frac{\partial}{\partial t}\mathbf{A}_{\text{drive}}^*, \quad (\text{A9})$$

where asterisks denote the Fourier components.

In the component form Eq. (A9) is a 3×3 linear system, which can be written as

$$\frac{\partial \mathbf{v}^*}{\partial t} = L(\mathbf{k})\mathbf{v}^* + \frac{\partial}{\partial t}\mathbf{A}_{\text{drive}}^*, \quad (\text{A10})$$

where

$$L(\mathbf{k}) = \frac{1}{1 + k^2} \begin{pmatrix} -\nu k^2 + k_x k_y & -k^2 + k_x^2 & 0 \\ k^2 - k_y^2 & -\nu k^2 - k_x k_y & 0 \\ -k_y k_z & k_x k_z & -\nu k^2 \end{pmatrix} \quad (\text{A11})$$

is the system matrix and $k^2 = k_x^2 + k_y^2 + k_z^2$, while \mathbf{v}^* and $\mathbf{A}_{\text{drive}}^*$ are treated as column vectors. Solution of Eq. (A10) can be written in the form

$$\mathbf{v}^*(\mathbf{k}, t) = U(\mathbf{k})e^{\Lambda(\mathbf{k})t} \left(U^{-1}(\mathbf{k})\mathbf{v}^*(\mathbf{k}, 0) + \int_0^t e^{-\Lambda(\mathbf{k})t'} U^{-1}(\mathbf{k}) \frac{\partial}{\partial t'} \mathbf{A}_{\text{drive}}^*(\mathbf{k}, t') dt' \right), \quad (\text{A12})$$

where $\Lambda(\mathbf{k})$ and $U(\mathbf{k})$ are diagonal matrix of eigenvalues and modal matrix that consists of columns of corresponding eigenvectors, which decompose the system matrix [Eq. (A11)] as

$$L = U\Lambda U^{-1} \quad (\text{A13})$$

and do not depend on time. Thus, for a given geometry they can be computed only once. Particularly, in the case of harmonically driven field and zero initial plasma current we get

$$\frac{\partial}{\partial t}\mathbf{A}_{\text{drive}}^*(\mathbf{k}, t) = \mathbf{F}^*(\mathbf{k})e^{i\omega t}, \quad \mathbf{v}^*(\mathbf{k}, 0) = 0, \quad (\text{A14})$$

and Eq. (A12) transforms into

$$\mathbf{v}^*(\mathbf{k}, t) = U(\mathbf{k})M(\mathbf{k}, t)U^{-1}(\mathbf{k})\mathbf{F}^*(\mathbf{k}), \quad (\text{A15})$$

where

$$M(\mathbf{k}, t) = (e^{\Lambda(\mathbf{k})t} - e^{i\omega t})(\Lambda(\mathbf{k}) - i\omega I)^{-1}, \quad (\text{A16})$$

where I is identity matrix.

To find the eigenvalues of $L(\mathbf{k})$ we need to solve characteristic equation which can be written in the form

$$\left[\left(\lambda + \frac{\nu k^2}{1 + k^2} \right)^2 + \left(\frac{k k_z}{1 + k^2} \right)^2 \right] \left(\lambda + \frac{\nu k^2}{1 + k^2} \right) = 0. \quad (\text{A17})$$

This gives us the eigenvalues

$$\lambda_{1,2} = -\frac{\nu k^2}{1+k^2} \mp i \frac{k k_z}{1+k^2}, \quad \lambda_3 = -\frac{\nu k^2}{1+k^2}. \quad (\text{A18})$$

The first pair of complex conjugate roots describes wave propagation in $\pm \mathbf{e}_z$ directions with frequency

$$\omega(\mathbf{k}) = -\text{Im}\{\lambda_{1,2}\} = \pm \frac{k k_z}{1+k^2} \quad (\text{A19})$$

and uniform attenuation

$$\text{Re}\{\lambda_3\} = \frac{\nu k^2}{1+k^2}. \quad (\text{A20})$$

The last eigenvalue describes purely decaying, nonpropagating mode. Finally we get the dispersion relation for the whistler waves,

$$\left(\omega + i \frac{\nu k^2}{1+k^2}\right)^2 = \left(\frac{k k_{\parallel}}{1+k^2}\right)^2, \quad (\text{A21})$$

which in the nondissipative case become

$$\omega = \frac{k k_{\parallel}}{1+k^2}. \quad (\text{A22})$$

This is the quasilongitudinal dispersion relation in Ref. 18 with $k_{\parallel} = k_z$. In the case of plane whistler waves propagating along the ambient magnetic field $k = k_{\parallel}$, that is, the wave vector \mathbf{k} has no transverse component ($k_{\perp} = 0$), we get the well-known whistler dispersion relation

$$\omega = \frac{k^2}{1+k^2}. \quad (\text{A23})$$

Equation (A22) can be rewritten as

$$\omega = \frac{k_{\parallel} \sqrt{k_{\parallel}^2 + k_{\perp}^2}}{1 + k_{\parallel}^2 + k_{\perp}^2}. \quad (\text{A24})$$

For k_{\parallel}^2 , Eq. (A24) has two solutions. One of them corresponds to the evanescent wave and plays significant role for the near field structure. The second root

$$k_{\parallel}^2 = \frac{-k_{\perp}^2 + 2(1+k_{\perp}^2)\omega^2 + \sqrt{k_{\perp}^4 + 4\omega^2(1+k_{\perp}^2)}}{2(1-\omega^2)} \quad (\text{A25})$$

corresponds to the propagating mode. To calculate the value of the longitudinal wavelength $\lambda_{\parallel} = 2\pi/k_{\parallel}$ we need to know the value of normal component of wave vector k_{\perp} , which is

mainly determined by the source of the radiation. For example, if we have an oscillating electric dipole oriented perpendicular to the ambient magnetic field its size will be roughly half the wavelength in the transverse direction. In the case of the magnetic dipole the perpendicular wavelength is also determined by the antenna size.

¹I. R. Jones, *Phys. Plasmas* **6**, 1950 (1999).

²A. L. Hoffman, *Nucl. Fusion* **40**, 1523 (2000).

³U. S. Inan, T. F. Bell, J. Bortnik, and J. M. Albert, *J. Geophys. Res.* **108**, 1186, doi:10.1029/2002JA009580 (2003).

⁴X. Shao, K. Papadopoulos, and A. S. Sharma, *J. Geophys. Res.* **114**, A07214, doi:10.1029/2009JA014066 (2009).

⁵T. H. Stix, *Waves in Plasmas* (AIP, New York, 1992).

⁶R. A. Helliwell, *Whistlers and Related Ionospheric Phenomena* (Stanford University Press, Stanford, CA, 1965).

⁷J.-A. Sauvaud, R. Maggiolo, C. Jacquey, M. Parrot, J.-J. Berthelier, R. J. Gamble, and C. J. Rodger, *Geophys. Res. Lett.* **35**, L09101, doi:10.1029/2008GL033194 (2008).

⁸R. Abel and R. M. Thorne, *J. Geophys. Res.* **103**, 2385, doi:10.1029/97JA02919 (1998).

⁹A. D. M. Walker, *Plasma Waves in the Magnetosphere* (Springer-Verlag, New York, 1993).

¹⁰A. Gigliotti, W. Gekelman, P. Pribyl, S. Vincena, A. Karavaev, X. Shao, A. S. Sharma, and D. Papadopoulos, *Phys. Plasmas* **16**, 092106 (2009).

¹¹W. Gekelman, H. Pfister, Z. Lucky, J. Bamber, D. Leneman, and J. E. Maggs, *Rev. Sci. Instrum.* **62**, 2875 (1991).

¹²J. R. Wait, *Electromagnetics and Plasmas* (Holt, Rinehart and Winston, New York, 1968).

¹³*Plasma Waves in Space and in the Laboratory*, edited by J. O. Thomas and B. J. Landmark (American Elsevier, New York, 1969).

¹⁴R. L. Stenzel, *Phys. Rev. Lett.* **35**, 574 (1975).

¹⁵T. N. C. Wang and T. F. Bell, *Radio Sci.* **5**, 605, doi:10.1029/RS005i003p00605 (1970).

¹⁶T. N. C. Wang and T. F. Bell, *Rev. Phys. Appl.* **7**, 11 (1972).

¹⁷T. F. Bell, U. S. Inan, and T. Chevalier, *Radio Sci.* **41**, RS2009, doi:10.1029/2005RS003260 (2006).

¹⁸A. V. Streltsov, M. Lampe, W. Menheimer, G. Ganguli, and G. Joyce, *J. Geophys. Res.* **111**, A03216, doi:10.1029/2005JA011357 (2006).

¹⁹P. Baille, J.-S. Chang, A. Claude, R. M. Hobson, G. L. Ogram, and A. W. Yau, *J. Phys. B* **14**, 1485 (1981).

²⁰J. M. Anderson and L. Goldstein, *Phys. Rev.* **100**, 1037 (1955).

²¹T. N. C. Wang, and T. F. Bell, *J. Geophys. Res.* **77**, 1174, doi:10.1029/JA077i007p01174 (1972).

²²I. G. Kondrat'ev, A. V. Kudrin, and T. M. Zaboronkova, *Radio Sci.* **27**, 315, doi:10.1029/91RS02919 (1992).

²³V. L. Ginzburg, *The Propagation of Electromagnetic Waves in Plasmas* (Pergamon, Oxford, 1964).

²⁴A. S. Kingsep, K. V. Chukbar, and V. V. Yankov, *Rev. Plasma Phys.* **16**, 243 (1990).

²⁵A. V. Gordeev, A. S. Kingsep, and L. I. Rudakov, *Phys. Rep.* **243**, 215 (1994).

²⁶M. Lampe, G. Joyce, W. M. Manheimer, A. Streltsov, and G. Ganguli, *J. Comput. Phys.* **214**, 284 (2006).

Physics of Plasmas is copyrighted by the American Institute of Physics (AIP). Redistribution of journal material is subject to the AIP online journal license and/or AIP copyright. For more information, see <http://ojps.aip.org/pop/popcr.jsp>